Interseismic deformation and creep along the central section of the North Anatolian Fault (Turkey): InSAR observations and implications for rate-and-state friction properties

Y. Kaneko,[1] Y. Fialko,[1] D. T. Sandwell,[1] X. Tong,[1] and M. Furuya[2]

[1]   We present high-resolution measurements of interseismic deformation along the central section of the North Anatolian Fault (NAF) in Turkey using interferometric synthetic aperture radar data from the Advanced Land Observing Satellite and Envisat missions. We generated maps of satellite line-of-sight velocity using five ascending Advanced Land Observing Satellite tracks and one descending Envisat track covering the NAF between 31.2°E and 34.3°E. The line-of-sight velocity reveals discontinuities of up to ∼5 mm/yr across the Ismetpasa segment of the NAF, implying surface creep at a rate of ∼9 mm/yr; this is a large fraction of the inferred slip rate of the NAF (21–25 mm/yr). The lateral extent of significant surface creep is about 75 km. We model the inferred surface velocity and shallow fault creep using numerical simulations of spontaneous earthquake sequences that incorporate laboratory-derived rate and state friction. Our results indicate that frictional behavior in the Ismetpasa segment is velocity strengthening at shallow depths and transitions to velocity weakening at a depth of 3–6 km. The inferred depth extent of shallow fault creep is 5.5–7 km, suggesting that the deeper locked portion of the partially creeping segment is characterized by a higher stressing rate, smaller events, and shorter recurrence interval. We also reproduce surface velocity in a locked segment of the NAF by fault models with velocity-weakening conditions at shallow depth. Our results imply that frictional behavior in a shallow portion of major active faults with little or no shallow creep is mostly velocity weakening.

Citation: Kaneko, Y., Y. Fialko, D. T. Sandwell, X. Tong, and M. Furuya (2013), Interseismic deformation and creep along the central section of the North Anatolian Fault (Turkey): InSAR observations and implications for rate-and-state friction properties, *J. Geophys. Res. Solid Earth*, *118*, doi:10.1029/2012JB009661.

1.   Introduction

[2]   Studies of interseismic strain accumulation on major active faults are critical for our understanding of fault mechanics as well as seismic hazard estimation. A majority of active faults are locked in the so-called seismogenic depth interval and release accumulated strain during large earthquakes. The extent of the seismogenic zone can vary between different faults and along the same fault. Observations show that aseismic fault slip, or fault creep, occurs in the upper crust on some segments of major faults including the San Andreas Fault (SAF) north of Parkfield [e.g., *Thatcher*, 1979; *Burford and Harsh*, 1980], the Hayward fault [e.g.,

Titus et al., 2006], the Superstition Hills fault [e.g., *Bilham*, 1989; *Wei et al.*, 2009], and the North Anatolian Fault (NAF) [e.g., *Ambraseys*, 1970; *Cakir et al.*, 2005]. If faults creep throughout the seismogenic layer at a rate comparable to the long-term fault slip rate, there is no accumulation of potential energy of elastic deformation and stress increase, and such faults are not likely to generate large earthquakes. For some faults, the observed rate of surface creep is lower than the long-term fault slip rate, implying that the creep may be limited to shallow depths, and that the deeper fault section is locked and accumulating elastic stress over time. Hence, the rate and spatial extent of fault creep are important parameters for seismic hazard estimation.

[3]   The occurrence of fault creep can further inform us of the frictional behavior of faults. Theoretical studies and ample laboratory observations suggest that the mechanism of fault creep is linked to steady-state velocity-strengthening behavior that, in the framework of rate-and state-dependent friction, allows only stable sliding in response to tectonic loading [e.g., *Ruina*, 1983; *Rice and Ruina*, 1983; *Marone et al.*, 1991; *Marone*, 1998]. Steady state rock friction exhibits either velocity weakening or velocity strengthening, depending on a number of factors including normal stress, temperature, and the rock type [e.g., *Dieterich*, 1978; *Ruina*, 1983;

[1] Institute of Geophysics and Planetary Physics, Scripps Institution of Oceanography, Univerisity of California, San Diego, La Jolla, California, USA.

[2] Department of Natural History Sciences, Graduate School of Science, Hokkaido University, Kita-ku, Sapporo, Japan.

Corresponding author: Y. Kaneko, Institute of Geophysics and Planetary Physics, Scripps Institution of Oceanography, University of California, San Diego, 9500 Gilman Dr. MC 0225, La Jolla, CA 92093, USA. E-mail: (ykaneko@ucsd.edu)

Blanpied et al., 1995; *Marone*, 1998; *Dieterich*, 2007]. Models predict that velocity-strengthening fault regions would slip stably under slow tectonic loading, whereas velocity-weakening fault regions would produce "stick-slip" motion [e.g., *Tse and Rice*, 1986; *Rice*, 1993; *Boatwright and Cocco*, 1996; *Kaneko et al.*, 2010]. In this framework, fault segments that creep aseismically can be interpreted to be dominantly velocity strengthening while locked patches are dominantly velocity weakening.

[4] Based on the rate-and-state concept, opposing views of friction properties at shallow depths (<2–3 km) have emerged. Friction properties at shallow depths are commonly considered to be velocity strengthening, based on laboratory experiments on fault gouge at low normal stress [e.g., *Marone et al.*, 1991; *Blanpied et al.*, 1995]. Because velocity-strengthening friction does not allow for spontaneous nucleation of frictional instabilities, the occurrence of shallow afterslip following some earthquakes [e.g., *Marone et al.*, 1991; *Bilham*, 1989] and the lack of seismicity at shallow depths [e.g., *Shearer et al.*, 2005] can be also interpreted as observational evidence for velocity-strengthening behavior of rocks in the uppermost crust.

[5] On the other hand, a majority of active faults appear to be locked near the Earth's surface, implying that frictional properties are mostly velocity weakening. Rock friction experiments by *Biegel et al.* [1989] show a transition from velocity strengthening to velocity weakening for shear displacements in excess of a few millimeters, suggesting that velocity-weakening behavior in the top few kilometers may be expected for mature strike-slip faults. Additional complexities are predicted by numerical models: velocity-strengthening segments can be locked due to elastic interactions with the adjacent velocity-weakening regions [e.g., *Kaneko et al.*, 2010; *Hetland and Simons*, 2010] and parts of velocity-weakening segments can experience aseismic slip [e.g., *Tse and Rice*, 1986; *Liu and Rice*, 2005]. Hence,

inferences of friction properties of major active faults from a combination of field measurements and models incorporating rate-and-state friction may clarify the frictional behavior of the shallow crust [e.g., *Johnson et al.*, 2006; *Barbot et al.*, 2009].

[6] In this paper, we investigate interseismic deformation and shallow fault creep along the central section of the NAF in Turkey. The NAF is a major active right-lateral strike-slip fault in northern Anatolia that constitutes the boundary between the Eurasian plate and the Anatolian plate (Figure 1). A sequence of eight $M > 7$ earthquakes ruptured ~900 km of the NAF from 1939 to 1999 [e.g., *Sengör et al.*, 2005], posing significant earthquake hazard in Turkey. The NAF is in many ways similar to the SAF in California; both are mature strike-slip faults extending more than 1000 km and having a total offset of the order of 10^2 kilometers [*Stein et al.*, 1997]. The long-term fault slip rate of the NAF of 22 ± 3 mm/yr [e.g., *McClusky et al.*, 2000] is close to that of the southern SAF [e.g., *Johnson et al.*, 1994; *Fialko*, 2006; *Lindsey and Fialko*, 2012]. Both faults also have segments with robust surface creep [e.g., *Irwin*, 1990; *Ambraseys*, 1970; *Cakir et al.*, 2005; *Karabacak et al.*, 2011]. On the NAF, the most notable creeping segment is located near Ismetpasa (Figure 1). *Cakir et al.* [2005] estimated the rate and spatial extent of the Ismetpasa creeping segment using interferometric synthetic aperture radar (InSAR) data from the ERS satellite spanning a time period from 1992 through 2001. Their InSAR data yield 8 ± 3 mm/yr of creep rate, suggesting that the NAF at Ismetpasa does not creep at seismogenic depth, unlike the creeping segment of the SAF north of Parkfield.

[7] Our study consists of two parts: (1) high-resolution measurements of interseismic deformation and fault creep based on InSAR and GPS data and (2) inferences of fault-rheological parameters in the upper crust based on comparisons of numerical simulations and the geodetic observations. We present satellite line-of-sight (LOS) velocity maps for the five
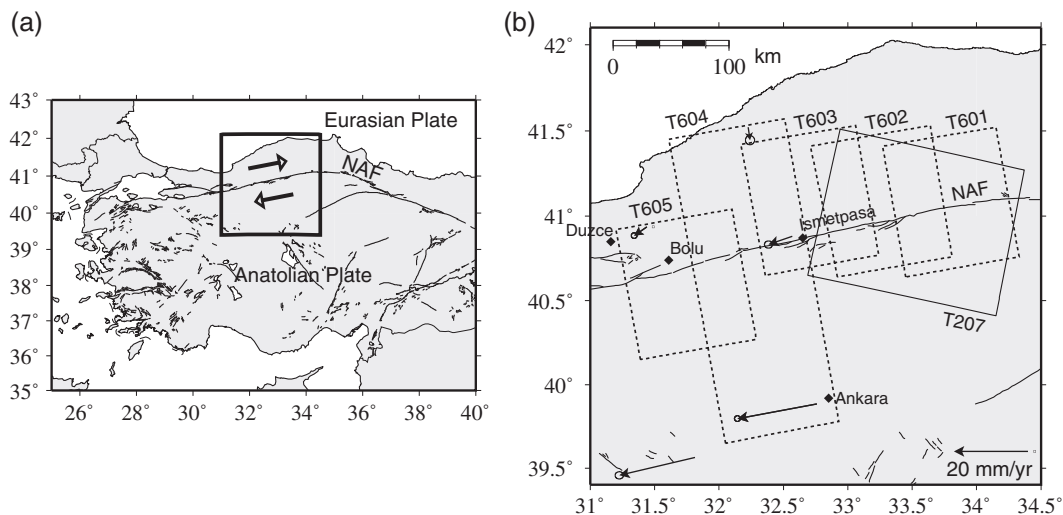

Figure 1. (a) Map of Turkey and the surrounding areas. The NAF runs along the transform boundary between the Eurasian plate and the Anatolian plate. Fault traces are from geological studies [*Arpat and Saroglu*, 1972, 1975]. Our focus region is indicated by a rectangle. (b) Map of a study region. Footprints of ALOS tracks 601–605 and Envisat track 207 used in this study are indicated by rectangles. Five GPS velocity vectors in a Eurasia-fixed reference frame and 1-σ confidence ellipses from *Reilinger et al.* [2006] are shown. Diamonds denote major cities in this region.

ascending tracks of Advanced Land Observing Satellite (ALOS) covering the NAF between 31.2°E and 34.3°E (section 2). LOS velocity maps for each track were obtained by averaging 10 to 20 radar interferograms spanning a time period of 4 years between 2007 and 2011. We also analyzed radar interferograms from the descending track 207 of Envisat satellite in roughly the same time period. The obtained surface velocity was used to infer spatial variations of fault friction properties based on simulations of spontaneous earthquake sequences that incorporate laboratory-derived rate-and-state friction laws [*Lapusta et al.*, 2000; *Kaneko et al.*, 2011]. We explore trade-offs between model parameters in section 3. Finally, in section 4 we discuss factors that are not included in the model but could be relevant for the inferences of fault friction properties in the uppermost crust.

2. InSAR and GPS Observations

2.1. Surface Velocity

[8] Our focus region is the central section of North Anatolian Fault (Figure 1). Most of the Synthetic Aperture Radar (SAR) data used in this study were collected by the ALOS from five ascending tracks 601–605 over a period of 4 years from the beginning of 2007 to the beginning of 2011 (Figure 1b). The use of a longer radar wavelength in the ALOS satellite (*L*-band, 23.6 cm), compared to that used in the ERS and Envisat satellites (*C*-band, 5.6 cm), enables

coherent phase recovery over much longer time intervals in vegetated areas such as those in northern Turkey [*Wei and Sandwell*, 2010].

[9] There are some campaign GPS data available in the vicinity of the NAF [*Reilinger et al.*, 2006]. Unfortunately, many of the GPS sites are located to the west of our study area; only five GPS data points are available within the radar swaths used in this study (Figure 1b). Nevertheless, these GPS data are a useful complement to the InSAR data because the former can be used to minimize the long-wavelength errors in the InSAR range changes. Here we used a crude GPS-based model (see the inset of Figure 2) to correct for the long-wavelength (>80 km) errors in the LOS velocity (Appendix A). From the GPS data, the long-term relative plate motion across the NAF in this area is 23±2 mm/yr [*Reilinger et al.*, 2006]. Details of processing of the InSAR data and integration of a GPS-based model into InSAR surface velocity are described in Appendix A and *Tong et al.* [2012].

[10] Figure 2 shows high-resolution interseismic velocity across the NAF inferred from a stack of ALOS interferograms. Warm colors (positive velocities) correspond to areas that are moving away from the satellite, and cool colors (negative velocities) correspond to areas that are moving toward the satellite, consistent with expected right-lateral plate motion in this region. A creeping fault segment is characterized by a discontinuity in LOS velocity, indicated by a
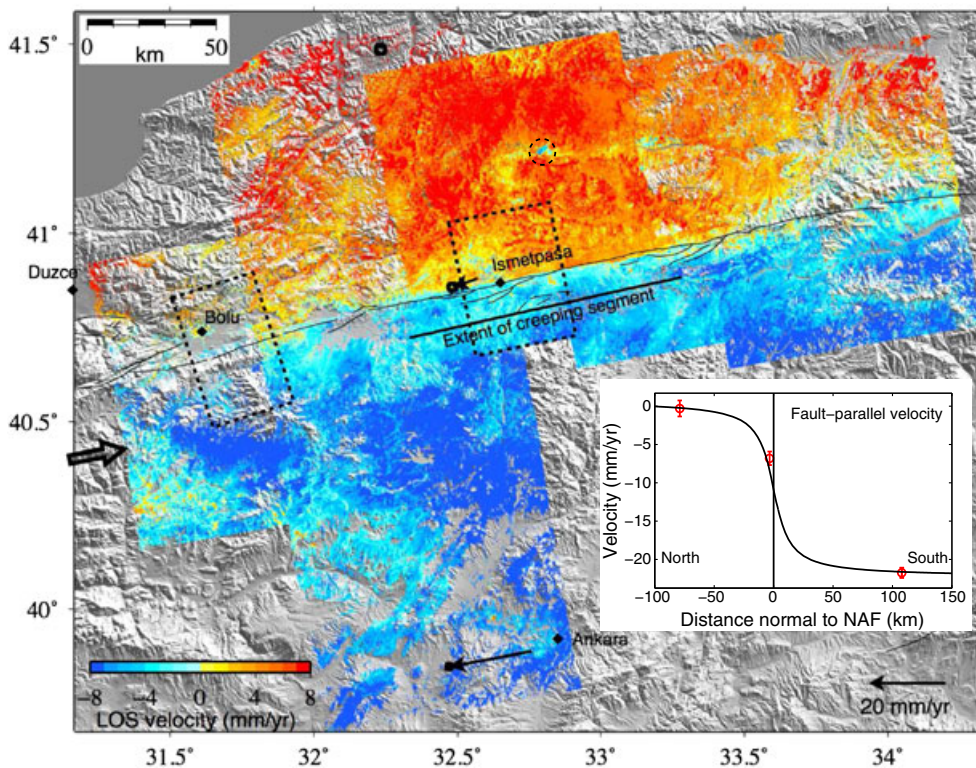

Figure 2. LOS velocity of the Earth's surface from a stack of ALOS radar interferograms spanning a time interval between 2007 and 2011. An open arrow shows the radar look direction, and LOS velocities away from the satellite are assumed to be positive. A thick solid line shows the extent of significant surface creep estimated in this study. Three GPS velocity vectors in a Eurasia-fixed reference frame and 1-σ confidence ellipses from *Reilinger et al.* [2006] are shown. The inset shows that the GPS data points and a curve used for constraining long-wavelength LOS velocity of the InSAR data.

sharp color contrast across the fault trace near Ismetpasa (Figure 2). In contrast, locked fault segments are manifested by gradual changes in the LOS velocity (e.g., the fault segment near Bolu, Figure 2).

[11] Other first-order variations in the interseismic velocity include localized deformation patterns related to nontectonic effects. There are several areas of rapid localized uplift or subsidence, possibly due to groundwater pumping or extraction. For example, there is a 1.5 km by 3 km uplift region (41.22° latitude, 32.80° longitude) located at about 40 km north of Ismetpasa (indicated by a dashed circle in Figure 2). The rate of the uplift is ∼10 mm/yr, likely of anthropogenic origin. The LOS velocity also includes noise associated with ionospheric effects, which are prominent in the wavelengths between ∼40 and ∼80 km. Hence, we limit our analysis of interseismic deformation to a region within ±20 km from the NAF, as discussed in section 3.

[12] In addition to the data from the ascending tracks of the ALOS satellite, we generated and analyzed 20 interferograms from the descending track 207 of the Envisat (Figure 1b). Envisat data were acquired between 2004 and 2010. Figure 3 shows surface velocity across the NAF inferred from stacking of the Envisat interferograms. Due to a shorter wavelength of the *C*-band radar, the Envisat interferograms are severely decorrelated due to erosion, vegetation, cultivation, etc. However, these data are important because they provide a

LOS velocity component from a different look direction, and allow us to resolve an ambiguity in the range changes due to vertical and horizontal motion [e.g., *Fialko et al.*, 2001, 2005]. Most variations in the LOS velocity shown in Figure 3 are likely to be associated with non-tectonic signals except for signature of shallow fault creep along the NAF. Hence, the Envisat surface velocity is used only for estimating the rate and lateral extent of the fault creep as discussed in the next section.

2.2. Fault Creep

[13] Based on the surface velocity from the InSAR observations, we estimate the rate and lateral extent of fault creep in the Ismetpasa segment. We adopt the method described by *Burford and Harsh* [1980] in which the creep rate is quantified as an offset of the intercepts of the two best fit linear approximations of surface velocity at the fault trace. To do this, we first need to know accurate locations of fault traces in the creeping segment of the NAF. Because the geologically-mapped fault traces shown in Figure 2 are found to be misaligned with discontinuities in the LOS velocity, sometimes by as much as 1 km, we compute across-the-fault gradient of the LOS velocity and define the fault trace as the location of the largest gradient in the vicinity of the geologically-mapped fault traces. We then take 1 km wide profiles of the averaged LOS velocity
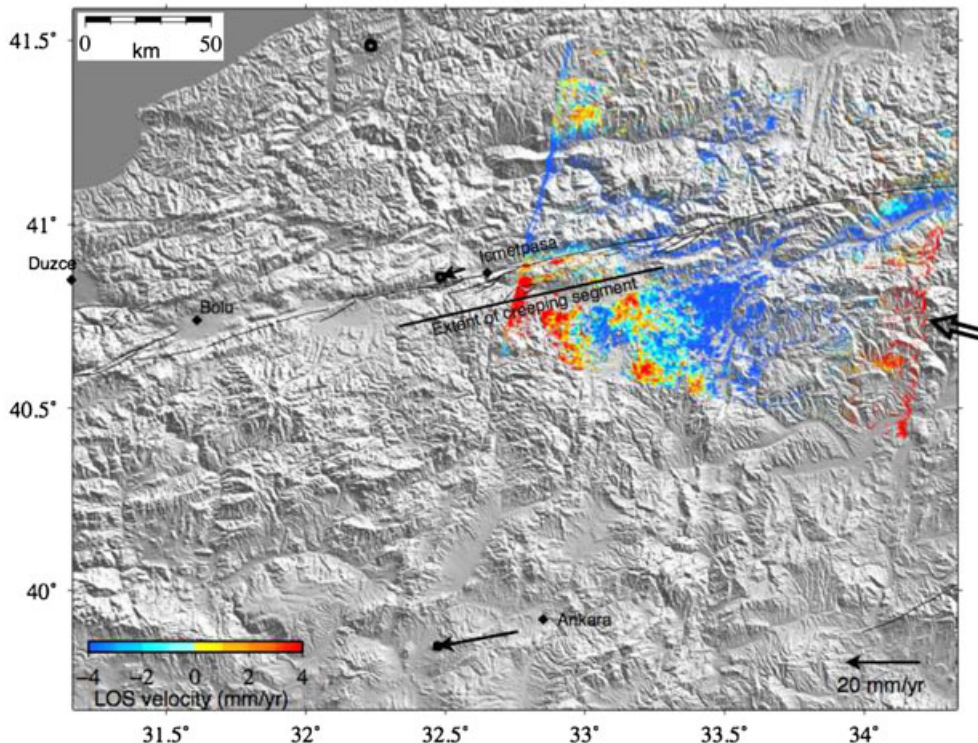

Figure 3. LOS velocity of the Earth surface from a stack of Envisat radar interferograms spanning a time interval between 2004 and 2010. For Envisat data, we do not use the InSAR/GPS integration method described in the text. Instead, the best fitting plane is removed from the LOS velocity field and the residual is shown here. An open arrow shows the radar look direction, and LOS velocities away from the satellite are assumed to be positive. A thick solid line shows the extent of significant surface creep estimated in this study. Three GPS velocity vectors in a Eurasia-fixed reference frame and 1-σ confidence ellipses from *Reilinger et al.* [2006] are shown.
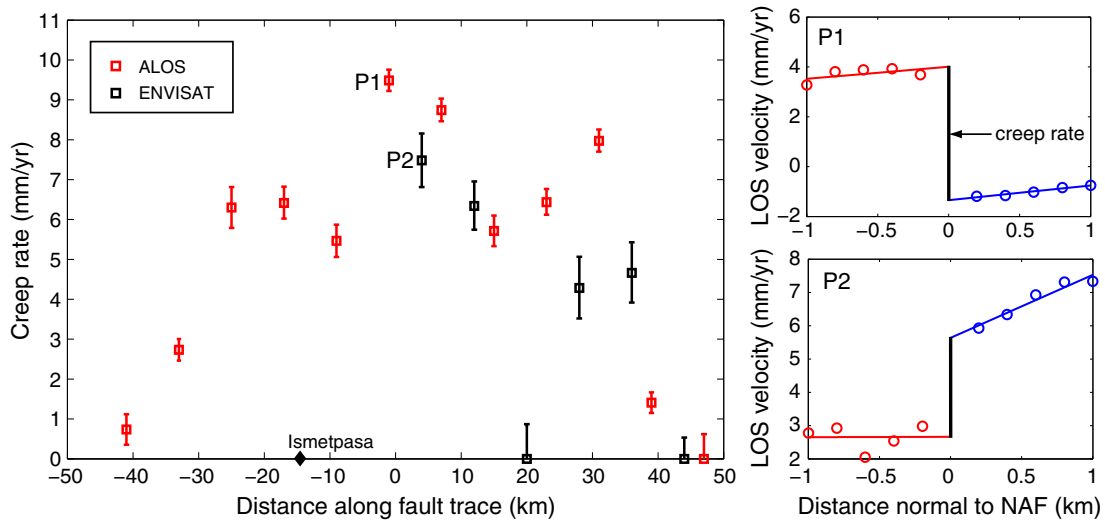
Figure 4. Creep rates estimated from profiles of averaged LOS velocity perpendicular to the fault in the Ismetpasa (creeping) section. Two examples of LOS velocities in 8 km averaged profiles and the best-fitting lines for data points in each side of the fault are shown (P1 from ALOS and P2 from Envisat). Error bars indicate 1-standard deviation of the root-mean-square (RMS) residuals after the linear regression for data points in each side of the fault. Offsets at the location of the fault trace (the lengths of the black lines) projected onto the fault parallel direction correspond to the estimated creep rates.

perpendicular to local fault strike. The sampling interval across the fault is 0.2 km for 1 km on either side of the fault. We further average the LOS velocity of 8 neighboring profiles along fault strike. For each averaged profile, there were 5 LOS velocity data points on either side of the fault (Figure 4). We project LOS velocity into a fault-parallel direction, assuming that there is no vertical and fault-normal motion. The error bars in Figure 4 correspond to the root-mean-square residuals from linear regression in averaged fault-normal profiles.

[14] The creep rates estimated from the ALOS and Envisat interferograms are generally similar in most locations (Figure 4). Since the LOS directions in the ascending ALOS and descending Envisat tracks are different, a general agreement of the creep rates from these estimates suggests that the differential vertical motion across the fault, if any, is negligible compared to the contribution from the right-lateral fault creep. Some profiles show apparent asymmetry in the LOS velocity across the fault trace (Profile P2 in Figure 4), which is likely due to the residual atmospheric noise. The maximum creep rate of up to ~9 mm/yr is found in the center of the creeping segment 10–20 km west of Ismetpasa, which accounts for 40% of the relative plate motion in this area (Figure 4a). The lateral extent of significant shallow creep is in excess of 75 km, and neighboring fault sections do not exhibit shallow creep within the measurement accuracy (1–2 mm/yr). These inferences are broadly consistent with previously reported trilateration surveys and InSAR results based on *C*-band ERS data [*Cakir et al*., 2005], suggesting that the NAF segment near Ismetpasa may be only partially locked.

[15] Discontinuities in the LOS velocities seen in Figures 2 and 3 are due to fault creep, and not atmospheric or other kinds of noise because observations from overlapping satellite tracks are consistent (see Figure 4). Also, the observed velocity variations do not generally correlate with local topography in the study area.

3. Dynamic Models of Earthquake Cycles and Interseismic Deformation

[16] To infer the depth extent of fault creep, one may use models of elastic dislocations to invert surface velocity for a locking depth [e.g., *Savage and Lisowski*, 1993]. Although this is a simple approach commonly used in interpreting geodetic data, an unphysical stress singularity exists at the dislocation edge defined by the discontinuity in slip. Also, the dislocation model offers little insight into the frictional properties of rocks comprising the fault zone. Instead, we use fully dynamic models of an earthquake sequence [*Lapusta et al*., 2000; *Kaneko et al*., 2011; *Kaneko and Ampuero*, 2011] to interpret the observed InSAR surface velocity. This approach has the following characteristics: (1) Occurrence of fault creep is dictated by laboratory derived rate-and-state friction and elasticity, and hence there is no stress singularity at the locking depth. (2) Earthquakes are simulated as a part of spontaneously occurring earthquake sequences on a fault subjected to slow tectonic loading, which allows us to study naturally developing coseismic, postseismic, and interseismic slip with conditions before the nucleation originating from the previous history of fault slip rather than from arbitrarily selected prestress. (3) Once the surface velocity is explained by the forward model, key parameters of fault friction such as the depth extent of the velocity-strengthening and velocity-weakening layers can be inferred. (4) Models could be used to assess future earthquake patterns and fault creep behavior by assimilating information about past earthquakes and interseismic loading. (5) Because the number of free parameters is larger in the dynamic model than in the kinematic dislocation-based models, the solution is likely to be highly nonunique. In the following section, we first present models that explain the surface velocity inferred from the InSAR data. We then analyze trade-offs between the input parameters and discuss ways to overcome some intrinsic nonuniqueness.
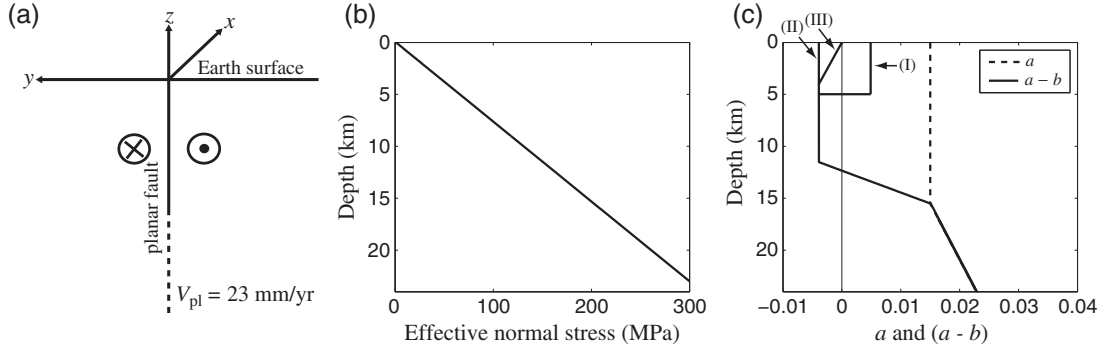
Figure 5. (a) 2-D model of a vertical strike-slip fault. (b) Depth-variable distribution of effective normal stress. (c) Depth-variable distributions of the rate-and-state constitutive parameters a and a - b over the fault segment where friction acts.

3.1. Model Setup

[17] We consider a vertical right-lateral strike-slip fault in a homogeneous half-space subjected to slow tectonic loading (Figure 5a). For simplicity, antiplane (two-dimensional, 2-D) deformation is assumed such that the only nonzero component of the displacement is the one along the x-direction and is given by $u(y, z, t)$, where t denotes time. We defined slip $\delta(z, t)$ on the fault place as the displacement discontinuity $\delta(z, t) = u(0^+, z, t)$ $u(0^-, z, t)$. Then the relation between slip $\delta(z, t)$, slip velocity V $(z, t) = \partial \delta(z, t) / \partial t$, and the corresponding shear stress $\tau(z, t)$ on the fault can be expressed as [*Lapusta et al.*, 2000]

$$\tau(z, t) \;=\; \tau^o(z) + f(z, t) - \frac{G}{2V_s} V(z, t) \; , \qquad (1)$$

where G is the shear modulus, V_s is the shear wave speed, τ^o is the loading stress that would act on the interface if it were constrained against any slip, and $f(z, t)$ is a linear functional of prior slip over the causality cone. The last term, known as radiation damping, is extracted from the functional $f(z, t)$ so that $f(z, t)$ can be evaluated without concern for singularities. The details of the elastodynamic solution and simulation methodology can be found in *Lapusta et al.* [2000]. The fault is driven below depth $z = -48$ km with a loading rate of $V_{pl} = 23$ mm/yr constrained by the GPS data (Figure 5a). The material properties are $V_s = 3.35$ km/s, $G = 30$ GPa, and density $\rho = 2670$ kg/m^3.

[18] The fault is governed by rate and state friction with the aging form of state variable evolution. For time-independent effective normal stress σ, the shear strength τ on the fault is expressed as

$$\tau(z, t) \;= \sigma(z) \left[f_o + a(z) \ln \frac{V(z, t)}{V_o} + b(z) \ln \frac{V_o \theta(z, t)}{L} \right]$$
$$\frac{d\theta(z, t)}{dt} \;= 1 - \frac{V(z, t)\theta(z, t)}{L}, \qquad (2)$$

where a and b are rate and state constitutive parameters, V is slip rate, f_o is the reference friction coefficient corresponding to the reference slip rate V_o, θ is a state variable, which can be interpreted as the average age of contacts between two surfaces, and L is the characteristic slip for state evolution [*Dieterich*, 1978, 1979; *Ruina*, 1983]. The parameter combination $a - b < 0$ corresponds to steady-state velocity-weakening friction and can lead to unstable slip, whereas $a - b > 0$ corresponds to steady-state velocity strengthening and leads to stable sliding [*Ruina*, 1983; *Rice and Ruina*, 1983].

[19] The actual fault resistance to sliding in our model is given by rate and state friction regularized at zero slip velocity, as described in Appendix B. The response of constitutive laws (2), when extrapolated to coseismic slip rates, becomes qualitatively similar to the one given by linear slip-weakening friction [*Cocco and Bizzarri*, 2011] widely used in dynamic rupture models [e.g., *Ida*, 1972; *Day et al.*, 2005]. For simplicity, we use the standard rate and state friction framework (2), without the inclusion of enhanced dynamic weakening at high slip rates [e.g., *Di Toro et al.*, 2003; *Rice*, 2006; *Noda and Lapusta*, 2010; *Brown and Fialko*, 2012].

[20] The physical parameters of the simulations presented in this work are shown in Figures 5b and 5c. The effective normal stress, $\sigma = 1.0 + 13.0z$ MPa, where z is in kilometers, increases with depth due to overburden (minus hydrostatic pore pressure, Figure 5b). The variation of friction parameters a and b with depth shown in Figure 5c is similar to the one in *Rice* [1993] and *Lapusta et al.* [2000]; it is derived from laboratory experiments [*Blanpied et al.*, 1995]. The transition from velocity weakening to velocity strengthening at 12.5 km depth is assumed to be associated with temperature increase with depth (Figure 5c). We experiment with different distributions of $a - b$ at shallow depths and how these distributions would affect the interseismic deformation and fault creep. The value of the characteristic slip L used in our simulations is 9 mm, in which case the model results in sequences of model-spanning earthquakes, consistent with the results of *Lapusta et al.* [2000] and *Kaneko et al.* [2011]. Our models resolve all stages of seismic and aseismic slip: the aseismic nucleation process, the subsequent inertially controlled earthquakes, the postseismic slip, and the interseismic deformation between earthquakes.

3.2. Modeling of Surface Velocity

[21] Figure 6 shows the evolution of simulated interseismic surface velocity compared to InSAR observations in the Ismetpasa creeping segment. The observed surface velocity profile (the red curve in Figure 6a) represents the average LOS velocity in a 25 km wide rectangle centered on the middle of the creeping segment (Figure 2). To compare the simulation against the observation, we first simulate an earthquake sequence (Figure 6b) and then take the corresponding surface
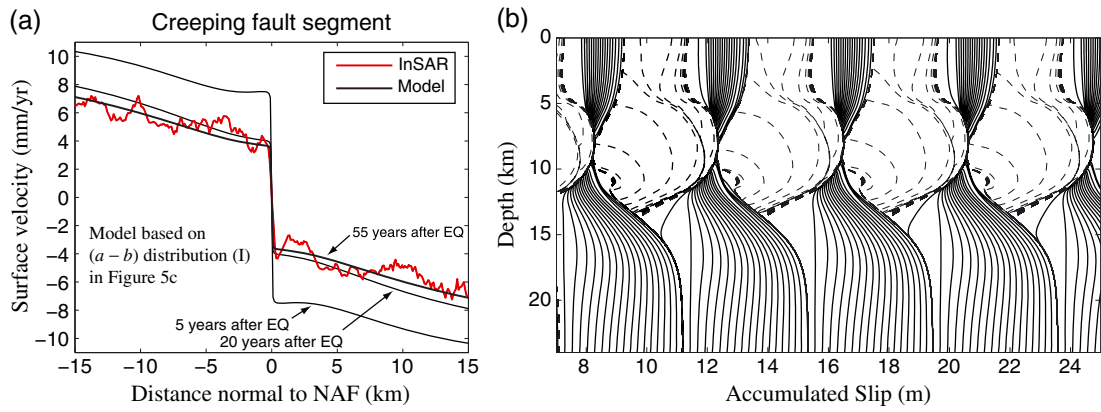
Figure 6. (a) Averaged surface velocity in the Ismetpasa creeping segment (a rectangle shown in Figure 2) and those computed from simulated interseismic slip-rate distributions shown in panel b. The interseismic surface velocities at 5, 20, and 55 years after a simulated earthquake are shown. (b) Simulated earthquake sequence with a shallow velocity-strengthening condition (Distribution I in Figure 5c). Solid lines show slip accumulation every 10 years, whereas dashed lines are intended to capture dynamic events and are plotted every second during the simulated earthquakes.
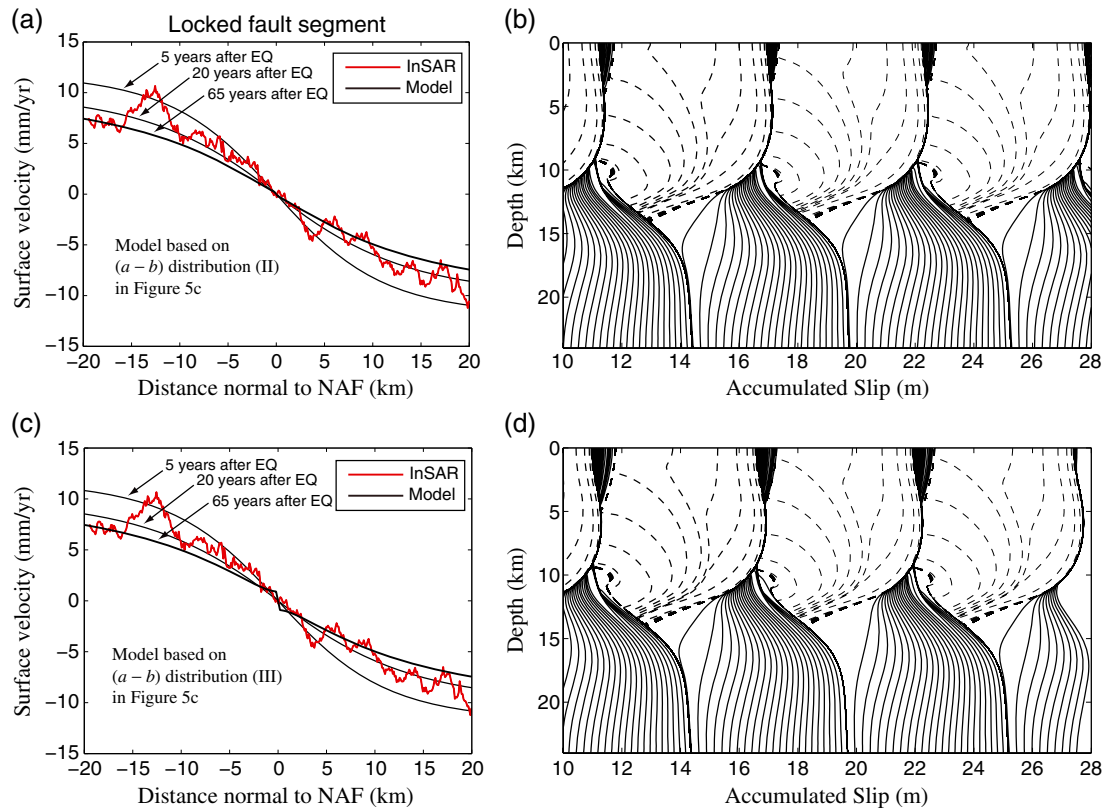

Figure 7. (a) Averaged surface velocity near the Bolu locked segment (a rectangle shown in Figure 2) and those computed from simulated interseismic slip-rate distributions shown in panel b. The interseismic surface velocities at 5, 20, and 55 years after a simulated earthquake are shown. (b) Simulated earthquake sequence with a shallow velocity-weakening condition (Distribution II in Figure 5c). Solid lines show slip accumulation every 10 years, whereas dashed lines are intended to capture dynamic events and are plotted every second during the simulated earthquakes. (c) Averaged surface velocity near the Bolu locked segment and those computed from simulated interseismic slip-rate distributions shown in Figure 7d. (d) Simulated earthquake sequence with a velocity-neutral condition at the Earth's surface (Distribution III in Figure 5c).

velocity at 55 years after a seismic event, because the last major earthquake on the Ismetpasa segment occurred in 1951 (the M6.9 Kursunlu earthquake) [*Ambraseys*, 1970; *Barka*, 1996]. The solid lines are plotted every 10 years and show the continuous slow sliding of the velocity-strengthening regions (Figure 6b). The slow slip creates a stress concentration at the tip of the slipping area and penetrates into the velocity-weakening region. In due time, an earthquake nucleates at an 11 km depth close to the deeper velocity-weakening and velocity-strengthening transition. We show the progression of seismic slip with dashed lines plotted every second (Figure 6b). The interseismic period between two successive events is ~180 years. The simulated creep rate is highest after an earthquake and logarithmically decays over time (Figure 6a), and the corresponding surface velocity evolves over time during the subsequent interseismic period.

[22] The model with a particular choice of $a - b$ distribution (Distribution I in Figure 5c) is used to reproduce the spatial distribution and the magnitude of a discontinuity of ~8 mm/yr in the InSAR surface velocity (Figure 6a). We run a sweep of simulations with different distributions of $a - b$ in the shallow depth interval and find the case that best reproduces the InSAR surface velocity profile. In this model, the total slip at the Earth surface over an earthquake cycle is partitioned into 50% coseismic slip, 20% postseismic afterslip, and 30% interseismic creep (Figure 6b). The coseismic surface rupture qualitatively agrees with paleoseismological observations in that historical major earthquakes did rupture the Earth's surface in this area [*Kondo et al.*, 2004]. The inferred value of $a - b = 0.005$ in the top 5 km depth interval falls into the range of measured laboratory values for various rock types with velocity-strengthening properties [*Reinen et al.*, 1994; *Marone*, 1998].

[23] We also model InSAR surface velocity in the Bolu segment (Figure 2). Because the NAF in this segment is locked near the Earth's surface, there is no resolvable discontinuity in LOS velocity (the red curve in Figure 7a). To reproduce this observation, we consider the case with a velocity-weakening condition in the top 5 km (Distribution II of $a - b$ in Figure 5c). Because the last major slip event on this segment was the 1944 M7.3 Bolu-Gerede earthquake [*Ambraseys*, 1970; *Kondo et al.*, 2004], we use simulated surface velocity at 65 years after the previous earthquake (Figures 7a and 7b). In this case, the simulated surface velocities at 20 and 65 years after the previous earthquake both agree fairly well with the InSAR surface velocity.

[24] To examine the sensitivities of rate-and-state parameters on surface velocity in the locked region, we also consider a case with velocity-neutral condition, $a - b = 0$, at the Earth's surface (Distribution III of $a - b$ in Figure 5c). We find that such change in the distribution of $a - b$ has almost no influence on the pattern of the simulated earthquakes (Figures 7b and 7d), but the amount of interseismic creep increases slightly (Figures 7a and 7c). As a result, the fault creeps at a rate of 2 mm/yr at 65 years after the previous earthquake in the velocity-neutral case (Figure 7c). We note that the measurement accuracy of the InSAR data is 1–2 mm/yr, suggesting that the case with velocity-neutral condition cannot be completely ruled out. The spatial variation of $a - b$ in the locked segment can be better constrained from more accurate InSAR (or other geodetic) observations.

3.3. Trade-off Between Friction Parameter $a - b$ and the Thickness of a Velocity-Strengthening Layer

[25] As discussed earlier, simulated surface velocity in the dynamic model is nonunique, that is, the same surface velocity
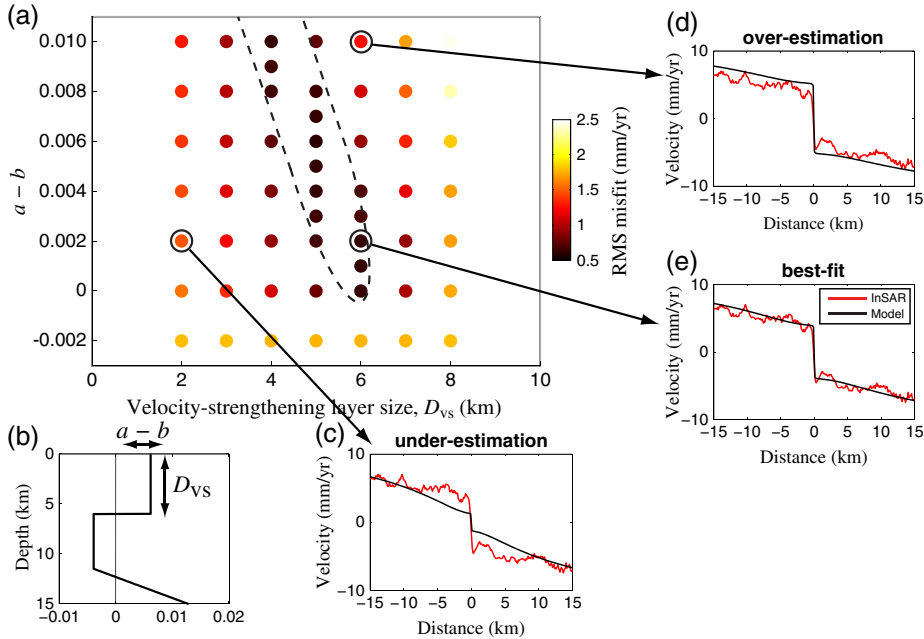

Figure 8. (a) Dependence of an RMS misfit between simulated surface velocity and InSAR data on the friction property $a - b$ and the size of a velocity-strengthening layer D_{vs}. A dashed curve encircles models with small RMS misfits. (b) Depth-variation distribution of $a - b$. Arrows correspond to the parameters varied in Figure 8a. (c–e) Three specific examples of simulated surface velocity, which are compared with the InSAR surface velocity shown in Figure 6a.
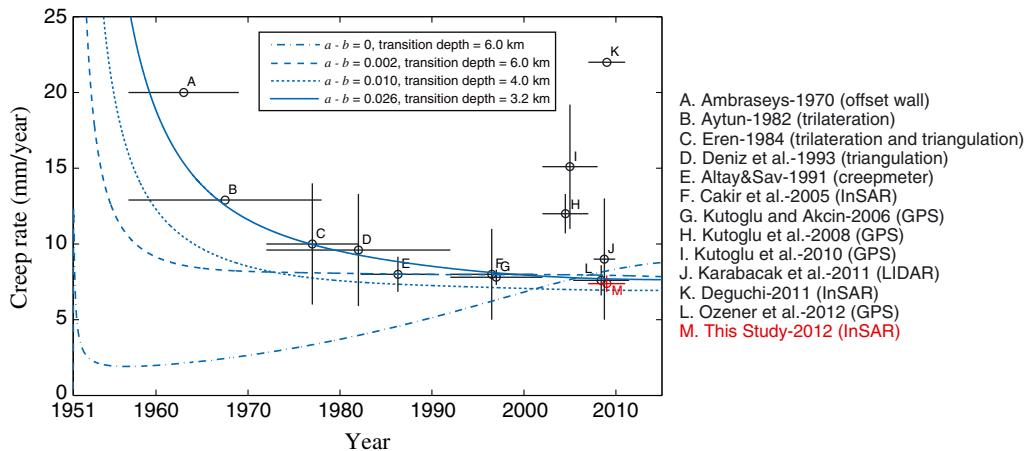
Figure 9. Comparison of simulated creep rates over time with creep rates in the Ismetpasa segment reported in various studies. Simulated creep rates for three cases with small RMS misfits shown in Figure 8a and an additional case with $a - b = 0.026$ and $a = 0.030$ in the shallow velocity-strengthening layer are shown. The timings of simulated earthquakes are aligned with that of the last major earthquake (1951 M6.9 Kursunlu) in this segment. Horizontal and vertical bars represent the monitoring time window and the error range, respectively. The error range was not reported in some studies and hence only the monitoring times are shown.

can be reproduced by models with different sets of parameters. To understand the uncertainties in the inferred parameters, we run a number of simulations with different combinations of the velocity-strengthening parameter $a - b$ and the layer size D_{vs} and quantify how they influence the misfit between modeled and InSAR surface velocity (Figure 8). When $a - b$ and D_{vs} are large, the model overestimates the creep rate from the InSAR velocity (Figure 8b). Conversely, smaller a-b and D_{vs} result in underestimation of the creep rate (Figure 8c). The InSAR surface velocity in the creeping segment is reproduced by models with larger $a - b$ given smaller D_{vs} and vice versa (Figure 8e), and hence there are many scenarios that can explain the InSAR surface velocity equally well (parameter range encircled by a dashed curve in Figure 8a).

[26] The non-uniqueness of the creep rate in the dynamic models can be understood from the following simple analysis. The amount of fault creep during an earthquake cycle in rate-and-state models would be proportional to the resistance C of a velocity-strengthening layer to seismic slip:

$$C \propto \sigma_{av}(a - b)D_{vs}, \qquad (3)$$

where σ_{av} is the effective normal stress averaged over the velocity-strengthening layer and D_{vs} is the layer size (Appendix C). A larger value of either σ_{av}, a-b, or D_{vs} would lead to smaller coseismic slip and hence a larger amount of fault creep and a higher creep rate, which is consistent with the simulation results in Figure 8. This also means that tradeoffs exist among these three parameters, which are not generally well constrained from observations.

3.4. Evolution of Creep Rates Over Time

[27] To further constrain the inferred friction parameters and the size of the velocity-strengthening layer among the cases with small misfits, we compare the simulated evolution of creep rates to the reported creep rates at Ismetpasa from previous studies (Figure 9) [*Ambraseys*, 1970; *Aytun*,
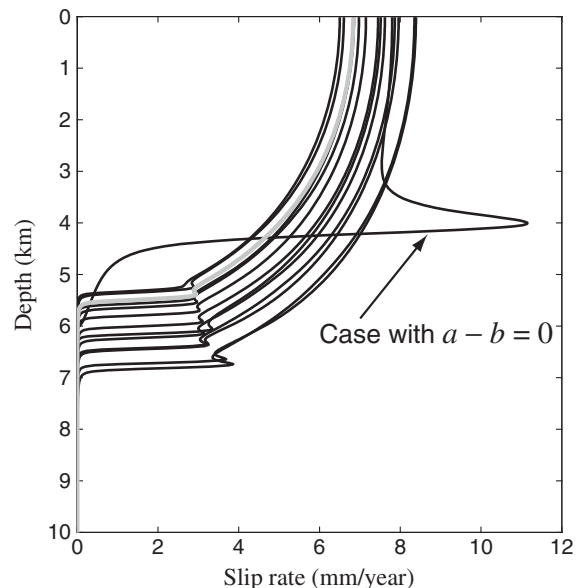

Figure 10. Distributions of slip rates in the models with small misfits (all the cases encircled by a dashed curve shown in Figure 8a) and an additional case with $a - b = 0.026$ and $a = 0.030$ (grey curve) shown in Figure 9. Extent of shallow fault creep for the good-fitting cases ranges from 5.5 to 7 km. The slip-rate distribution for the velocity-neutral case ($a - b = 0$) is different from that for other cases, suggesting that the nearfield InSAR data cannot resolve the distribution of slip rates greater than ~3 km depth.

1982; *Eren*, 1984; *Altay and Sav*, 1991; *Deniz et al.*, 1993; *Cakir et al.*, 2005; *Kutoglu and Akcin*, 2006; *Kutoglu et al.*, 2008, 2010; *Karabacak et al.*, 2011; *Deguchi*, 2011; *Ozener et al.*, 2012]. Estimated creep rates reported in the previous studies were based on conventional surveying methods, GPS, LiDAR, or InSAR techniques (Figure 9),

and their results are summarized in *Ozener et al.* [2012]. Available observations suggest that the rate of creep at Ismetpasa is nearly constant (within the measurement errors) since 1970, which would eliminate the case with a velocity-neutral condition (a - b = 0). Assuming that the creep rate estimated by tape-meter [*Ambraseys*, 1970] is robust, the time-dependent creep rates favor the model with a larger a - b and a smaller velocity-strengthening layer among the cases with smaller misfits shown in Figure 8a. To better reproduce the time-dependent creep rates, we considered an additional model with $a − b = 0.026$, which predicts a gradual change in the surface creep rate from 12 to 7.5 mm/yr since 1970, although uncertainties in observations may be too large to distinguish between these models (Figure 9). The slower decay of the creep rate in this case can be understood from the result of *Perfettini and Avouac* [2004] from which the duration of the creep rate in a velocity-strengthening layer is proportional to $\sigma(a − b)$; larger $\sigma(a − b)$ results in slower decay of the creep rate after an earthquake.

3.5. Depth Extent of the Shallow Fault Creep

[28] A depth extent of shallow creep, or a creep depth in the dynamic models is generally time-dependent and slowly increases as creep fronts penetrate into the velocity-weakening zone during the interseismic period (e.g., Figure 6b). Nevertheless, we find that creep depths in the dynamic models appear to be relatively independent of the parameter trade-offs discussed above. Figure 10 shows simulated slip-rate distributions for the cases with small misfits (Figure 8a). Slip rates in these models are always nonzero mathematically but spatially vary over orders of magnitude. Hence, the creep depth can be visually identified from Figure 10. Creep depths from those cases range from 5.5 to 7.0 km, consistent with the previous inference of a creep depth in the Ismetpasa segment [*Cakir et al.*, 2005]. This result suggests that the deeper locked portion of the partially creeping segment, compared to that of locked segments, is characterized by a higher stressing rate, smaller events, and shorter recurrence interval, as manifested by the differences between Figures 6b and 7b. Such inference is consistent with a suggestion that fault segments with a higher stressing rate have shorter recurrence intervals [*Smith-Konter and Sandwell*, 2009].

[29] A recent seismological study of *Ozakin et al.* [2012] proposed that the stressing rate at the seismogenic depth is not higher in the Ismetpasa segment than in the surrounding regions. *Ozakin et al.* [2012] found that only a small number of earthquakes were detected in the Ismetpasa segment, unlike the creeping segment of the SAF north of Parkfield. If the fault creeps down to a depth of 5.5–7 km, it is perhaps surprising that only a small number of events occur at the Ismetpasa segment. An alternative explanation may be that heterogeneities on the fault surface have been swept away by the ruptures of the 1944 and 1951 earthquakes, leading to the scarcity of small earthquakes in this region.

4. Discussion

[30] Observations of surface deformation on different segments of the NAF indicate that the friction properties in the uppermost crust vary along fault strike. Our results suggest that friction properties of creeping fault segments are mostly velocity strengthening, whereas locked fault segments are characterized by mostly velocity-weakening conditions at shallow depths. This simplified concept is illustrated in Figure 11. If a fault creeps at a long-term slip rate as in the center of the Parkfield segment of the SAF, the fault surface is characterized by velocity-strengthening conditions. A shallow portion of locked faults is nominally velocity weakening as in the Bolu locked segment because velocity-strengthening or velocity-neutral conditions would lead to shallow fault creep at some time in the interseismic period (Figure 7). The Ismetpasa segment of the NAF corresponds to the intermediate behavior (Figure 11) where the friction parameter in the shallow portion of the fault is velocity strengthening but transitions to velocity weakening at a greater depth (Figure 6).

[31] Because a majority of active faults appear to be locked near the Earth surface or creep at an unresolvable rate, our results imply that friction properties at shallow depths are generally velocity weakening, contrary to the view that unconsolidated fault gouge due to low effective normal stress results in velocity strengthening [*Marone et al.*, 1991; *Blanpied et al.*, 1995]. Rock friction experiments by *Biegel et al.* [1989] show a reduction in a - b and a transition from velocity strengthening to velocity weakening for shear displacements in excess of millimeters. *Beeler et al.*
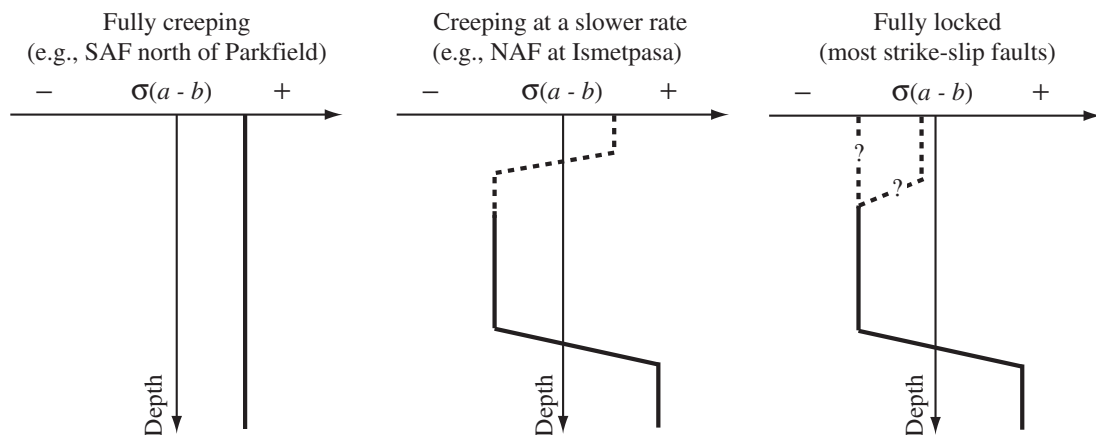

Figure 11. Simplified view on distributions of friction parameter $\sigma(a − b)$ for crustal strike-slip faults with different interseismic creep rates at the Earth surface.

[1996] argued that in the presence of fault gouge, the frictional behavior is velocity strengthening even for large displacements. For the San Andreas Fault drilling site at a 3 km depth located near the creeping strand of the SAF, fault creep is thought to occur due to the presence of weak clay minerals that exhibit velocity-strengthening behavior [*Carpenter et al.*, 2011]. One possibility is that the Ismetpasa segment of the NAF may host different fault-zone materials at shallow depths (<3–6 km), similar to the SAF around the San Andreas Fault Observatory at Depth drilling site.

[32] In modeling surface velocity, we have made several simplifying assumptions, which may have affected the inferences of fault friction properties along the NAF. In the following, we discuss factors that are not included in our models but could be relevant for the inferences of fault friction properties in the uppermost crust.

4.1. Recurrence Interval of Major Earthquakes

[33] One of the main simplifications made in the dynamic model is that the friction parameters are chosen such that the model results in sequences of large quasi-characteristic earthquakes. For the model shown in Figure 6b, the resulting recurrence interval is ∼180 years. Paleoseismological studies suggest that four major earthquakes occurred with quite irregular recurrence intervals in the Ismetpasa segment of the NAF: 1035, 1668, 1944, and 1951 A.D. [*Ambraseys*, 1970; *Kondo et al.*, 2004]. The irregularity likely reflects heterogeneities in slip distributions of those earthquakes, postseismic afterslip, interseismic creep, and interseismic stressing rates, all of which are poorly constrained by the existing paleoseismological data [*Ambraseys*, 1970; *Kondo et al.*, 2004]. Intrinsic trade-offs between poorly-constrained model parameters shown in section 3 can be alleviated by using those additional data as constraints for dynamic models.

4.2. Effects of Three-dimensional Geometry

[34] In this study, we use 2-D models of spontaneous dynamic rupture that assume no variations of slip or friction properties along the fault strike. The spatial variation of the creep rates along the NAF in Figure 4 suggests that the depth extent of the shallow creep varies spatially and that the greatest depth extent of the shallow creep is located around the center of the creeping segment. In this case, the depth extent of shallow creep inferred from the 2-D models would be underestimated; the actual creep depth may be greater than the inferred depth of 5.5–7 km. In addition, the adjacent locked fault regions can suppress the magnitude of creep in the shallow velocity-strengthening segment, which may result in underestimation of the friction parameters inferred from the 2-D models. The same argument applies to the inferred size of the shallow velocity-strengthening layer; the actual location of the velocity-strengthening to velocity-weakening transition may be deeper than 3–6 km.

4.3. Loading Due to Viscoelastic Relaxation in the Lower Crust

[35] In our dynamic models, the fault is driven below depth $z = -48$ km with a loading rate of $V_{pl} = 23$ mm/yr (Figure 5a). An alternative mode of interseismic loading is viscoelastic relaxation in the lower crust and upper mantle from past earthquakes [e.g., *Savage and Prescott*, 1981]. We note that deformation in the top of the seismogenic layer is essentially independent of the mechanism of interseismic loading, as long as the models fit the observed velocity field. Furthermore, viscoelastic models that take into account laboratory-derived rheologies and long-term deformation predict development of localized shear zones in the ductile substrate [*Takeuchi and Fialko*, 2012]. Such shear zones are kinematically similar to a deep dislocation that imitates tectonic loading in this study.

4.4. Enhanced Dynamic Weakening at Coseismic Slip Rates

[36] There is growing evidence that friction may be much lower at seismic slip velocities than rate and state friction laws predict [e.g., *Di Toro et al.*, 2003; *Han et al.*, 2007; *Rice*, 2006; *Noda and Lapusta*, 2010; *Brown and Fialko*, 2012, and references therein]. In this study, we assume that the fault constitutive response is represented by the rate and state friction formulation without accounting for the enhanced weakening at seismic slip rates of the order of 1 m/s. Our models are still capable of simulating inertially controlled seismic slip with realistic slip velocities and rupture speeds. Yet, the recent study of *Noda and Lapusta* [2011] that used models incorporating additional coseismic weakening shows different behavior and interactions of seismic and aseismic slip. Their results suggest that steady-state velocity-strengthening regions can weaken during seismic slip due to high slip rates and stresses at the rupture tip. In the subsequent interseismic period, the velocity-strengthening region would exhibit "apparent" locking for some time during the strength recovery, followed by the onset of creep. In this case, frictional behavior of locked fault segments can be velocity-strengthening in steady-state conditions even though there is no creep in some periods of time.

[37] Such scenario may be a way to reconcile laboratory observations of steady state velocity strengthening behavior at low-confining pressure with the relative scarcity of shallow fault creep. The key question in validating this model is whether time-dependent behavior of fault locking and creeping is generally observed over an earthquake cycle. Because many locked faults are presumably at different stages of earthquake cycles, the scarcity of fault creep observations imply that such enhanced coseismic weakening is not dominant in the shallow portion of faults due to possibly the presence of thicker gouge or distributed deformation near the Earth surface [e.g., *Hamiel and Fialko*, 2007; *Kaneko and Fialko*, 2011]. Further observations of long-term time-dependent fault creep behavior are needed to better constrain in situ frictional properties of rocks comprising the slip interface, and the behavior of major crustal faults throughout the seismic cycle.

5. Conclusions

[38] We have investigated interseismic deformation and shallow fault creep along the central section of the NAF using InSAR data collected by the ALOS and Envisat satellites, and GPS observations. The LOS velocity fields reveal

discontinuities of up to ~5 mm/yr across the Ismetpasa segment of the NAF, indicating surface creep at a rate up to ~9 mm/yr; this is a large fraction of the inferred fault slip rate (21–25 mm/yr). The lateral extent of significant surface creep is about 75 km, broadly consistent with results of previous studies [*Cakir et al*., 2005]. Neighboring fault sections do not exhibit shallow creep within the measurement accuracy (1–2 mm/yr). Better coherence in the *L*-band ALOS interferograms in our study area, compared to the *C*-band Envisat interferograms, has enabled better recovery of phase associated with small-scale ground deformation, such as fault creep.

[39] Using fully dynamic models of earthquake cycles, we reproduce the surface velocity and shallow fault creep estimated from InSAR data. Our results indicate that frictional behavior in the Ismetpasa segment is velocity strengthening at shallow depths and transitions to velocity weakening at a depth of 3–6 km. The inferred depth extent of the shallow fault creep at Ismetpasa is 5.5–7 km, suggesting that the deeper locked portion of the partially creeping segment is characterized by a higher stressing rate, smaller events and shorter recurrence interval. In modeling the variation of locking and creeping fault behavior along the NAF, the friction parameter $a - b$ at shallow depths vary along the fault strike: the creeping segment is characterized by nominally velocity-strengthening conditions ($a - b > 0$), whereas the locked faults are nominally velocity weakening ($a - b < 0$) or velocity neutra ($a - b = 0$). This conclusion should generally apply to all active faults that lack shallow creep throughout the interseismic period.

[40] We have found that the dynamic models that incorporate rate-and-state friction combined with geodetic observations of interseismic deformation due to mature active faults can be used to infer in situ rate-state parameters of seismogenic crust. Intrinsic trade-offs between poorly-constrained model parameters can be alleviated by using additional data, such as slip distributions from past earthquakes, postseismic afterslip, interseismic creep, and interseismic stressing rates. The recent study by *Barbot et al*. [2012] came to a similar conclusion by developing a fully dynamic model of the Parkfield segment of the San Andreas Fault that reproduces interseismic, coseismic, and postseismic observations. Such calibrated physical models may provide constraints on in situ fault-friction parameters and ways to quantitatively assess seismic hazards due to major crustal faults.

Appendix A: Data Processing— Integration of InSAR and GPS Data

[41] We process five ascending tracks of ALOS PALSAR acquisitions spanning the time period from the beginning of 2007 to the beginning of 2011 using GMTSAR software, publicly available at http://topex.ucsd.edu/gmtsar [*Sandwell et al*., 2011]. Figures A1 and A2 show catalogs of radar acquisitions from the ascending ALOS satellite tracks 601–605 and the descending Envisat track 207, respectively.

Radar interferograms used in this study are denoted by lines in Figures A1 and A2. Several radar acquisitions not used in this study have either missing data, unfavorable baselines or problems with decorrelation or ionospheric noise (i.e., variations of electron content in the ionosphere). The main processing steps consist of (1) preprocessing, (2) SAR image formation and alignment, (3) forming interferograms and topographic phase correction, (4) phase unwrapping, and (5) InSAR/GPS integration. Steps (1) through (4) are described in a standard SAR processing software [*Sandwell et al*., 2011]. We processed the SAR data on a frame-by-frame basis to avoid discarding entire tracks of data when the pulse repetition frequency changes along track or the SAR data in one of the frames were missing or problematic. In step (5), we use an approach called "SURF" (<u>S</u>um/<u>R</u>emove/<u>Fil</u>ter/<u>R</u>estore) described in the study of *Tong et al*. [2012].

[42] The essence of InSAR/GPS integration in step (5) is to correct for long-wavelength errors of InSAR phase data by (i) summing up interferograms to form a stack of LOS velocity, (ii) removing a GPS model from the stack, (iii) high-pass filtering the residual stack, and (iv) restoring the GPS model by adding it back to the filtered residual stack. In the following, we describe each step:

1. Sum up the properly selected sets of interferograms by keeping track of the total time span of the sum. After obtaining the time-averaged interferogram, we covert it to LOS velocity using an appropriate radar wavelength.
2. Remove an interseismic GPS model from the stacked phase to obtain the residual phase. Since there are only 5 campaign GPS data points in the study area (Figure 1b), we construct a crude GPS model based on 2-D elastic dislocations [*Okada*, 1992], which qualitatively fits the fault-parallel component of three GPS data points as shown in the inset of Figure 2. This GPS model is projected from geographic coordinates (longitude/latitude) into radar coordinates (range/azimuth) via spatially varying radar look directions across the track.
3. High-pass filter the residual phase. We use a Gaussian high-pass filter to filter out wavelengths longer than 80 km. Based on a coherence spectrum analysis of GPS models in California, *Tong et al*. [2012] found an optimal filter wavelength of the filter to be 40 km. Because the GPS model in this study is not very accurate over the entire area and we focus on the short-wavelength signal of LOS velocity, we set the cut-off wavelength to be 80 km.
4. Restore the GPS model by adding it back to the filtered residual phase. By this process, the LOS velocity is composed of the combination of the short-wavelength signal from InSAR stacking and the long-wavelength signal from GPS [*Tong et al*., 2012]. The cross-over wavelength is given by a wavelength of 80 km used in the high-pass filter in step 3.

[43] Stacking a large number of interferograms, in theory, reduces noise associated with nontectonic signals. Because only 10–20 interferograms are used for stacking in each track, the LOS velocity for the wavelength between ~40 and ~80 km (Figure 2) includes noise related to ionospheric effects. Hence, we focus our analysis on LOS velocity with the wavelengths shorter than 40 km.
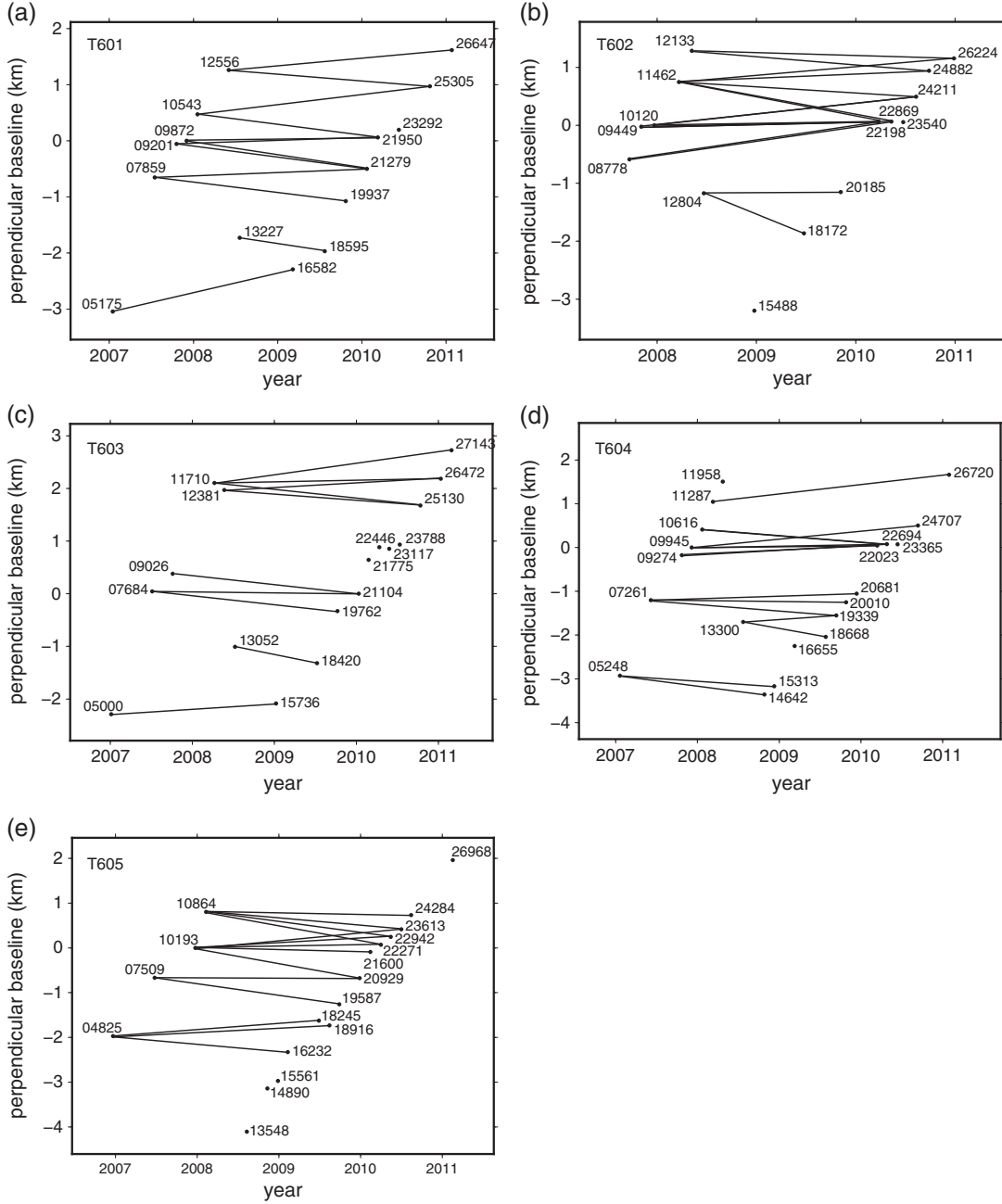
Figure A1. ALOS SAR data from the ascending tracks 601–605. Dots denote radar acquisition labeled by the orbit numbers. Horizontal axis represents time, and vertical axis represents perpendicular baseline (i.e., distance between repeated orbits). Lines indicate radar pairs used in this study.

Appendix B: Rate and State Friction Regularized at Zero Slip Velocity

[44] In expression (2), shear frictional strength τ is undefined for slip velocities $V = 0$, which is unphysical. To regularize (2) near $V = 0$, we follow the approach of *Rice and Ben-Zion* [1996] and *Lapusta et al.* [2000] in using a thermally activated creep model of the direct effect term $a ln(V/V_o)$ to obtain

$$\tau = a\sigma \ \mathrm{arcsinh}\left[\frac{V}{2V_o}\exp\left(\frac{f_o + b\ln(V_o\theta/L)}{a}\right)\right]. \quad (B1)$$

This regularization produces a negligible change from equation (2) in the range of slip velocities explored by laboratory experiments; the difference in V at $V \sim V_o$ is of the order of $\exp(-2f_0/a)$ or less, and the typical value of f_0/a in this study is 40.

Appendix C: Derivation of a Parameter That Controls the Amount of Creep in the Velocity-strengthening Layer

[45] The amount of creep in the velocity-strengthening layer in an earthquake cycle can be understood from stress
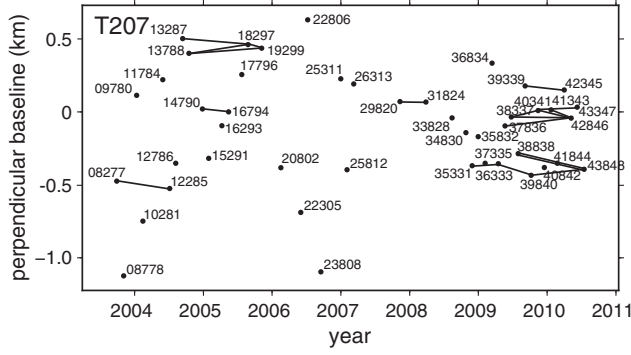
13

Figure A2. Envisat SAR data from the descending track 207. The dots and lines have the same meaning as in Figure A1.

increase required for the layer to sustain seismic slip [*Kaneko et al.*, 2010]. During an earthquake, the stress is transferred from a velocity-weakening region to the adjacent velocity-strengthening layer. Let us consider the stress increase required for the velocity-strengthening layer to sustain seismic slip integrated over the patch, $C = \Delta\tau_{prop}D_{vs}$, where $\Delta\tau_{prop}$ is the average required amount of shear stress increase and D_{vs} is the size of the velocity-strengthening layer. We refer to C as the velocity-strengthening layer resistance. To estimate $\Delta\tau_{prop}$, we consider the difference in shear stress on the velocity-strengthening patch before and during seismic slip. Prior to the arrival of seismic rupture, the shear stress on the velocity-strengthening layer is given by

$$\tau^i = \sigma\left[f_0 + (a-b)\ln\left(V^i/V_0\right)\right], \qquad (C1)$$

where V^i is the representative interseismic slip rate in the velocity-strengthening layer. During seismic slip with slip rate V^{dyn}, shear stress in the layer can be approximated as

$$\tau^d = \sigma\left[f_0 + (a-b)\ln\left(V^{dyn}/V_0\right)\right]. \qquad (C2)$$

Then

$$\Delta\tau_{prop} = \left|\tau^d - \tau^i\right| = \sigma(a-b)\ln\left(V^{dyn}/V^i\right). \qquad (C3)$$

V^{dyn} is of the order of the typical seismic slip velocity of 1 m/s, and V_i ranges from the plate velocity of 10^{-9} m/s to values smaller by 1–2 orders of magnitude, so that $\ln(V_{dyn}/V_{tecti}) \approx 20$, nearly independent of the model parameters. Therefore, the resistance to the seismic slip C is given by

$$C = 20\sigma(a-b)D_{vs} \propto \sigma(a-b)D_{vs}. \qquad (C4)$$

[46] For nonuniform distributions of $\sigma(z)$, $a(z)$, and $b(z)$, C can be calculated by

$$C = 20\int_{D_{vs}} \sigma(z)(a(z)-b(z))dz. \qquad (C5)$$

[47] The analysis above ignores the larger but shorter-lived stress increase at the rupture tip, which becomes progressively more important as a-b approaches zero; a velocity-neutral patch would still provide resistance to the rupture propagation through the breakdown work at the rupture tip. This effect can actually be incorporated with additions of more parameters [*Kaneko et al.*, 2010]. In this work, we ignore this additional contribution for simplicity.

References

Altay, C., and H. Sav (1991), Continuous creep measurement along the North Anatolian Fault zone, *Türk. Jeol. Kurumu Bült.*, 6, 77–84.

Ambraseys, N. N., Some characteristic features of the Anatolian fault zone, *Tectonophysics*, 9, 143–165, doi:10.1016/0040-1951(70)90014-4, 1970.

Arpat, E., and F. Saroglu (1972), The East Anatolian fault system: thoughts on its development, *Bull. Min. Res. Expl. Inst. Turkey*, 78, 33–39.

Arpat, E., and F. Saroglu (1975), Turkiye deki bazi onemli genc Tektonik olaylar, *Türk. Jeol. Kurumu Bült.*, 18(1), 91–101.

Aytun, A. (1982), Creep measurements in the Ismetpasa region of the North Anatolian Fault zone, in A. M. Isikara, A. Vogel (Eds.), Proceedings, Multidisplinary Approach to Earthquake Prediction, Friedr. Vieweg and Sohn, Braunschweig/Wiesbaden, pp. 279–292.

Barbot, S., Y. Fialko, and Y. Bock (2009), Postseismic deformation due to the mw 6.0 2004 parkfield earthquake: Stress-driven creep on a fault with spatially variable rate-and-state friction parameters, *J. Geophys. Res.*, 114, B07,405.

Barbot, S., N. Lapusta, and J.-P. Avouac (2012), Under the hood of the earthquake machine: Toward predictive modeling of the seismic cycle, *Science*, 336, 707–710, doi:10.1126/science.1218796.

Barka, A. (1996), Slip distribution along the North Anatolian fault associated with the large earthquakes of the period 1939 to 1967, *Bull. Seismol. Soc. Am.*, 86(5), 1238–1254.

Beeler, N. M., T. E. Tullis, M. L. Blanpied, and J. D. Weeks (1996), Frictional behavior of large displacement experimental faults, *J. Geophys. Res.*, 101, 8697–8715, doi:10.1029/96JB00411.

Biegel, R. L., G. Sammis, and J. H. Dieterich (1989), *J. Struct. Geol.*, 11(7), 827–846, doi:10.1016/0191-8141(89)90101-6.

Bilham, R. (1989), Surface slip subsequent to the 24 November 1987 Superstition Hills, *Bull. Seismol. Soc. Am.*, 79, 424–450.

Blanpied, M. L., D. A. Lockner, and J. D. Byerlee (1995), Frictional slip of granite at hydrothermal conditions, *J. Geophys. Res.*, 100, 13,045–13,064, doi:10.1029/95JB00862.

Boatwright, J., and M. Cocco (1996), Frictional constraints on crustal faulting, *J. Geophys. Res.*, 101, 13,895–13,909.

Brown, K. M., and Y. Fialko (2012), "Melt welt" mechanism of extreme weakening of gabbro at seismic slip rates, *Nature*, 488, 638–641, doi: 10.1038/nature11370.

Burford, R. O., and P. W. Harsh (1980), Slip on the San Andreas fault in central California from alinement array surveys, *Bull. Seismol. Soc. Am.*, 79(4), 1233–1261.

Cakir, Z., A. M. Akoglu, S. Belabbes, S. Ergintav, and M. Meghraoui (2005), Creeping along the Ismetpasa section of the North Anatolian fault (Western Turkey): Rate and extent from InSAR, *Earth Planet. Sci. Lett.*, 238, 225–234, doi:10.1016/j.epsl.2005.06.044.

Carpenter, B. M., C. Marone, and D. M. Saffer (2011), Weakness of the San Andreas Fault revealed by samples from the active fault zone, *Nat. Geosci.*, 4, 251–254, doi:10.1038/ngeo1089.

Cocco, M., and A. Bizzarri (2011), On the slip-weakening behavior of rate and state dependent constitutive laws, *Geophys. Res. Lett.*, 29(11), doi:10.1029/2001GL013999.

Day, S. M., L. A. Dalguer, N. Lapusta, and Y. Liu (2005), Comparison of finite difference and boundary integral solutions to three-dimensional spontaneous rupture, *J. Geophys. Res.*, 110, B12307, doi:10.1029/2005JB003813.

Deguchi, T. (2011), Detection of fault creep around NAF by InSAR time series analysis using PALSAR data, In *Proceedings of SPIE 8179*, http://dx.doi.org/10.1117/12.898478, 81790.

Deniz, R., A. Aksoy, D. Yalin, H. Seeger, O. Hirsch, and P. Bautsch (1993), Determination of crustal movements in Turkey by terrestrial geodetic methods, *J. Geodyn.*, 18, 13–22.

Di Toro, G., D. L. Goldsby, and T. E. Tullis (2003), Friction falls towards zero in quartz rock as slip velocity approaches seismic rates, *Nature*, *427*, doi:10.1038/nature02249.

Dieterich, J. H. (1978), Time-dependent friction and the mechanics of stick-slip, *Pure Appl. Geophys.*, *116*, 790–806, doi:10.1007/BF00876539.

Dieterich, J. H. (1979), Modeling of rock friction: 1. Experimental results and constitutive equations, *J. Geophys. Res.*, *84*, 2,161–2,168, doi:10.1029/JB084iB05p02161.

Dieterich, J. H. (2007), Applications of rate- and state-dependent friction to models of fault slip and earthquake occurrence, *Treatise on Geophysics*, pp. 107–129, Elsevier, Amsterdam.

Eren, K. (1984), Strain analysis along the North Analtolian Fault by using geodetic surveys, *J. Geodesy*, *58*, 137–150, doi:10.1007/BF02520898.

Fialko, Y. (2006), Interseismic strain accumulation and the earthquake potential on the southern San Andreas fault system, *Nature*, *441*, 968–971, doi:10.1038/nature04797.

Fialko, Y., M. Simons, and D. Agnew (2001), The complete (3-D) surface displacement field in the epicentral area of the 1999 M_w7.1 Hector Mine earthquake, southern California, from space geodetic observations, *Geophys. Res. Lett.*, *28*, 3063–3066.

Fialko, Y., D. Sandwell, M. Simons, and P. Rosen (2005), Three-dimensional deformation caused by the Bam, Iran, earthquake and the origin of shallow slip deficit, *Nature*, *435*, 295–299, doi:10.1038/nature03425.

Hamiel, Y., and Y. Fialko (2007), Structure and mechanical properties of faults in the North Anatolian Fault system from InSAR observations of coseismic deformation due to the 1999 Izmit (Turkey) earthquake, *J. Geophys. Res.*, *112*, B07,412, doi:10.1029/2006JB004777.

Han, R., T. Shimamoto, T. Hirose, J.-H. Ree, and J. Ando (2007), Ultralow friction of carbonate faults caused by thermal decomposition, *Science*, *316*, doi:10.1126/science.1139763.

Hetland, E. A., and M. Simons (2010), Post-seismic and interseismic fault creep II: transient creep and interseismic stress shadows on megathrusts, *Geophys. J. Int.*, *181*, doi:10.1111/j.1365-246X.2010.04522.x.

Ida, Y. (1972), Cohesive force across the tip of a longitudinal-shear crack and griffith's specific surface energy, *J. Geophys. Res.*, *77*, 3796–3805, doi:10.1029/JB077i020p03796.

Irwin, W. P. (1990), Geology and plate tectonic development, in The San Andreas Fault System, California, USGS Open Prof. Pap. 1515, edited by R. E. Wallace, pp. 60–80, US Government Printing Office, Washington, DC.

Johnson, H. O., D. C. Agnew, and F. K. Wyatt (1994), Present-day crustal deformation in southern California, *J. Geophys. Res.*, *99*, 23,951–23,974.

Johnson, K. M., R. Bürgmann, and K. Larson (2006), Frictional properties on the San Andreas Fault near Parkfield, California, inferred from models of afterslip following the 2004 earthquake, *Bull. Seismol. Soc. Am.*, *96*, S321–S338.

Kaneko, Y., and J.-P. Ampuero (2011), A mechanism for preseismic steady rupture fronts observed in laboratory experiments, *Geophys. Res. Lett.*, *38*, doi:10.1029/2011GL049953.

Kaneko, Y., and Y. Fialko (2011), Shallow slip deficit due to large strike-slip earthquakes in dynamic rupture simulations with elasto-plastic off-fault response, *Geophys. J. Int.*, *186*, 1389–1403, doi:10.1111/j.1365-246X.2011.05117.x.

Kaneko, Y., J.-P. Avouac, and N. Lapusta (2010), Towards inferring earthquake patterns from geodetic observations of interseismic coupling, *Nat. Geosci.*, *3*, 363–369, doi:10.1038/NGEO843.

Kaneko, Y., N. Lapusta, and J.-P. Ampuero (2011), Spectral-element simulations of long-term fault slip: Effect of low-rigidity layers on earthquake-cycle dynamics, *J. Geophys. Res.*, *116*, doi:10.1029/2011JB008395.

Karabacak, V., E. Altunel, and Z. Cakir (2011), Monitoring aseismic surface creep along the North Anatolian Fault (Turkey) using ground-based LIDAR, *Earth Planet. Sci. Lett.*, *304*, 64–70, doi:10.1016/j.epsl.2011.01.017.

Kondo, H., Y. Awata, O. Emre, A. Dogan, S. Ozalp, F. Tokay, C. Yildirim, T. Yoshioka, and K. Okumura (2004), Slip Distribution, Fault Geometry, and Fault Segmentation of the 1944 Bolu-Gerede Earthquake Rupture, North Anatolian Fault, Turkey, *Bull. Seismol. Soc. Am.*, *95*, 1234–1249, doi:10.1785/0120040194.

Kutoglu, H. S., and H. Akcin (2006), Determination of the 30-year creep trend on the Ismetpasa segment of the North Anatolian Fault using an old geodetic network, *Earth Planets Space*, *58*(8), 937–942.

Kutoglu, H. S., H. Akcin, H. Kemaldere, and K. S. Gormus (2008), Triggered creep rate on the Ismetpasa segment of the North Anatolian Fault, *Nat. Hazards Earth Syst. Sci.*, *8*, 1369–1373.

Kutoglu, H. S., H. Akcin, O. Gundogdu, H. Kemaldere, and K. S. Gormus (2010), Relaxation on the Ismetpasa segment of the North Anatolian Fault after the Golcuk Mw = 7.4 and Duze Mw = 7.2 shocks, *Nat. Hazards Earth Syst. Sci.*, *10*, 2653–2657, 2010.

Lapusta, N., J. Rice, Y. Ben-Zion, and G. Zheng (2000), Elastodynamic analysis for slow tectonic loading with spontaneous rupture episodes on faults with rate- and state-dependent friction, *J. Geophys. Res.*, *105* (B10), 23,765–23,789, doi:10.1029/2000JB900250.

Lindsey, E., and Y. Fialko (2012), Geodetic slip rates in the Southern San Andreas Fault System: Effects of elastic heterogeneity and fault geometry, *J. Geophys. Res.*, in press, doi:10.1029/2012JB009358, 2013.

Liu, Y., and J. R. Rice (2005), Aseismic slip transients emerge spontaneously in 3D rate and state modeling of subduction earthquake sequences, *J. Geophys. Res.*, *110*, B08307, doi:10.1029/2004JB003424.

Marone, C. (1998), Laboratory-derived friction laws and their application to seismic faulting, *Annu. Rev. Earth Planet. Sci.*, *26*, 643–696, doi:10.1146/annurev.earth.26.1.643, 1998.

Marone, C., C. H. Scholz, and R. Bilham (1991), On the mechanics of earthquake afterslip, *J. Geophys. Res.*, *96*, 8,441–8,452, doi:10.1029/91JB00275.

McClusky, S., S. Balassanian, A. Barka, C. Demir, S. Ergintav, I. Georgiev, O. Gurkan, M. Hamburger, K. Hurst, H. Kahle, K. Kastens, G. Kekelidze, R. King, V. Kotzev, O. Lenk, S. Kekelidze, A. Mishin, M. Nadariya, A. Ouzounis, D. Paradissis, Y. Peter, M. Prilepin, R. Reilinger, I. Sanli, H. Seeger, A. Tealeb, M. N. Toksoz, and G. Veis (2000), Global Positioning System constraints on plate kinematics and dynamics in the eastern Mediterranean and Caucasus, *J. Geophys. Res.*, *105*(B3), 5695–5719, doi:10.1029/1999JB900351.

Noda, H., and N. Lapusta (2010), Three-dimensional earthquake sequence simulations with evolving temperature and pore pressure due to shear heating: Effect of heterogeneous hydraulic diffusivity, *J. Geophys. Res.*, *115*, B12314, doi:10.1029/2010JB007780.

Noda, H., and N. Lapusta (2011), Rich fault behavior due to combined effect of rate strengthening friction at low slip rates and coseismic weakening: implications for Chi-Chi and Tohoku earthquakes, *EOS Trans. Am. Geophys. Union*, fall Meeting 2011, abstract T42C-03.

Okada, Y. (1992), Internal deformation due to shear and tensile faults in a half-space, *Bull. Seismol. Soc. Am.*, *82*, 1018–1040.

Ozakin, Y., Y. Ben-Zion, M. Aktar, H. Karabulut, and Z. Peng (2012), Velocity contrast across the 1944 rupture zone of the North Anatolian fault east of Ismetpasa from analysis of teleseismic arrivals, *Geophys. Res. Lett.*, *39*, doi:10.1029/2012GL051426.

Ozener, H., A. Dogru, and B. Turgut (2012), Quantifying aseismic creep on the Ismetpasa segment of the North Anatolian Fault Zone (Turkey) by 6 years of GPS observations, *J. Geodyn.*, doi:10.1016/j.jog.2012.08.002.

Perfettini, H., and J.-P. Avouac (2004), Postseismic relaxation driven by brittle creep: A possible mechanism to reconcile geodetic measurements and the decay rate of aftershocks, applications to the Chi-Chi earthquake, Taiwan, *J. Geophys. Res.*, *109*, doi:10.1029/2003JB002488.

Reilinger, R., S. McClusky, P. Vernant, S. Lawrence, S. Ergintav, R. Cakmak, H. Ozener, F. Kadirov, I. Guliev, R. Stepanyan, M. Nadariya, G. Hahubia, S. Mahmoud, K. Sakr, A. ArRajehi, D. Paradissis, A. Al-Aydrus, M. Prilepin, T. Guseva, E. Evren, A. Dmitrotsa, S. V. Filikov, F. Gomez, R. Al-Ghazzi, and G. Karam (2006), GPS constraints on continental deformation in the Africa-Arabia-Eurasia continental collision zone and implications for the dynamics of plate interactions, *J. Geophys. Res.*, *111*, doi:10.1029/2005JB004051.

Reinen, L. A., J. D. Weeks, and T. E. Tullis (1994), The frictional behavior of lizardite and antigorite serpentinites: Experiments, constitutive models, and implications for natural faults, *Pure Appl. Geophys.*, *143*, 317–358, doi:10.1007/BF00874334.

Rice, J. R. (1993), Spatio-temporal complexity of slip on a fault, *J. Geophys. Res.*, *98*(B6), 9,885–9,907, doi:10.1029/93JB00191.

Rice, J. R. (2006), Heating and weakening of faults during earthquake slip, *J. Geophys. Res.*, *111*, doi:10.1029/2005JB004006.

Rice, J. R., and Y. Ben-Zion (1996), Slip complexity in earthquake fault models, *Proc. Natl. Acad. Sci. U.S.A.*, *93*, 3,811–3,818, doi:10.1073/pnas.93.9.3811.

Rice, J. R., and A. L. Ruina (1983), Stability of steady frictional slipping, *J. Appl. Mech.*, *50*, 343–349, doi:10.1115/1.3167042.

Ruina, A. L. (1983), Slip instability and state variable friction laws, *J. Geophys. Res.*, *88*, 10,359–10,370, doi:10.1029/JB088iB12p10359.

Sandwell, D., R. Mellors, X. Tong, M. Wei, and P. Wessel (2011), Open radar interferometry software for mapping surface deformation, *EOS Trans. Am. Geophys. Union*, *92*(28), 234, doi:10.1029/2011EO280002.

Savage, J., and M. Lisowski (1993), Inferred depth of creep on the Hayward fault, central California, *J. Geophys. Res.*, *98*, 787–793, doi:10.1029/92JB01871.

Savage, J. C., and W. H. Prescott (1981), Asthenosphere readjustment and the earthquake cycle, *J. Geophys. Res.*, *83*, 3369–3376.

Sengör, A. M. C., O. Tüysüz, C. Imren, M. Sakinc, H. Eyidogan, N. Görür, X. L. Pichon, and C. Rangin, (2005) The North Anatolian Fault: A new look, *Annu. Rev. Earth Planet. Sci.*, *33*, 37–112, doi:10.1146/annurev.earth.32.101802.120415.

Shearer, P. M., E. Hauksson, and G. Lin (2005), Southern California hypocenter relocation with waveform cross-correlation, Part 2: Results using source-specific station terms and cluster analysis, *Bull. Seismol. Soc. Am.*, *95*(3), 904–915.

Smith-Konter, B., and D. Sandwell (2009), Stress evolution of the San Andreas fault system: Recurrence interval versus locking depth, *Geophys. Res. Lett.*, *36*, doi:10.1029/2009GL037235.

Stein, R. S., A. A. Barka, and J. H. Dieterich (1997), Progressive failure on the North Anatolian fault since 1939 by earthquake stress triggering, *Geophys. J. Int.*, *128*(3), 594–604, doi:10.1111/j.1365-246X.1997.tb05321.x.

Takeuchi, C., and Y. Fialko (2012), Dynamic models of interseismic deformation and stress transfer from plate motion to continental transform faults, *J. Geophys. Res.*, *117*, doi:10.1029/2011JB009056.

Thatcher, W. (1979), Systematic Inversion of Geodetic Data in Central California, *J. Geophys. Res.*, *84*, 2283–2295, doi:10.1029/JB084iB05p02283.

Titus, S. J., C. DeMets, and B. Tikoff (2006), Thirty-five-year creep rates for the creeping segment of the San Andreas fault and the effects of the 2004 Parkfield eart hquake: Constraints from alignment arrays, continuous Global Positioning System, and creepmeters, *Bull. Seismol. Soc. Am.*, *96*, S250–S268, doi:10.1785/0120050811.

Tong, X., D. Sandwell, and B. Smith-Konter (2012), High-resolution interseismic velocity data along the san andreas fault from gps and insar, *J. Geophys. Res.*, submitted, doi:10.1029/2012JB009442, 2013.

Tse, S., and J. R. Rice (1986), Crustal Earthquake Instability in Relation to the Depth Variation of Frictional Slip Properties, *J. Geophys. Res.*, *91*(9), 452–9,472.

Wei, M., and D. Sandwell (2010), Decorrelation of ALOS and ERS interferometry over vegetated areas in California, *IEEE Geosci. Remote Sens.*, doi:10.1109/TGRS.2010.2043442.

Wei, M., D. Sandwell, and Y. Fialko (2009), A Silent M4.8 Slip Event of October 3-6, 2006, on the Superstition Hills Fault, Southern California, *J. Geophys. Res.*, doi: 10.1029/2008JB006135.